Fluid flow and fault-related subsurface fractures in slate and metasandstone formations: A case study of the Jentse Geothermal Area, Taiwan

Bing-Cheng Chen [a,b], Tito Perdana [c], Li-Wei Kuo [a,d,*]

[a] *Department of Earth Sciences, National Central University, Taoyuan, Taiwan*
[b] *Exploration & Production Business Division, CPC Corporation Taiwan, Taipei, Taiwan*
[c] *GeothermEx Inc, a Schlumberger Company, Richmond, CA, USA*
[d] *Earthquake-Disaster & Risk Evaluation and Management Center, National Central University, Taoyuan, Taiwan*

ARTICLE INFO

ABSTRACT

Permeable structures associated with faults are commonly treated as geothermal fluid conduits in most tight geothermal reservoirs. However, the properties of permeable structures within fault zones remain unclear due to the lack of subsurface geological data, e.g., the geothermal systems in the tight slate and metasandstone formations in Northeastern Taiwan. This study presented standard open-hole and Fullbore Formation MicroImager (FMI) logs acquired in the 8.5-inch-diameter section of the JT-3 well (800–1475 m measured depth) in the Jentse geothermal area, Taiwan, to identify the subsurface fracture structures and the possible pathway of fluid flow. Using open-hole log data, we generate a lithology interpretation for the borehole and model the associated effective porosity. Based on the FMI images, four types of natural open fractures, two types of natural sealed fractures, and drilling-induced tensile fractures were identified. Integration of the lithological model, the effective porosity, and the types of fractures reveals one major permeable fault system comprising three permeable fault zones. The fault system is composed of both permeable fault cores marked by porous fault breccia and damage zones characterized by a large number of open-fracture planes. The static borehole temperature log also shows deflections in these interpreted permeable fractures zone. Deflections in these fracture zones that, based on petrophysical and borehole image logs, are interpreted as permeable. According to the orientations of the bed boundaries and fault planes obtained from FMI images, the fault system may have an orientation of N50–70 °E and dips 70–90° to the NW with a width of around 116 m. This study illustrates how subsurface structures control geothermal conduits. The concept and workflow of this study may be useful for other fault-controlled geothermal areas in Taiwan.

1. Introduction

Geothermal energy is a renewable energy source that is produced by hot, circulating fluids in permeable geothermal reservoirs. Today, most geothermal power production is mainly from conventional hydrothermal areas, where primary permeability allows for the circulation of hot fluid in shallow porous reservoirs (Moeck, 2014). There are some geothermal systems mainly controlled by permeable geological structures (fractures or fault zones) within tight host rocks, such as the Basin and Range province of the US (Jolie et al., 2015), and the Hatchobaru geothermal system in Japan (Taguchi and Nakamura, 1991). These fault-related permeable structures are often narrow. It is difficult to predict their locations and properties if only limited geological or well data are available.

Fault zones may act as conduits, barriers, or combined conduit–barrier systems that either enhance or impede fluid flow depending on the properties of their internal structures. The internal structures of fault zones consist of fault cores and fault damage zones (Caine Jonathan et al., 1996; Rowland and Sibson, 2004). In some cases, fault cores are brecciated, which can lead to high permeability; in others, they are comprised of thick fine-grained fault gouges (e.g., Kuo et al., 2009, 2014, 2017) and behave as fluid barriers (Bense et al., 2013; Caine Jonathan et al., 1996; Faulkner et al., 2010; Houwers et al., 2015). Fault damage zones usually consist of intense fracture planes (e.g., Kuo et al., 2011). If these fracture planes remain open at the subsurface, they would also enhance fluid conductivity. The properties of the internal

---

structures of fault zones can be important factors controlling the development of permeable structures (Rawling et al., 2001; Taillefer et al., 2017; Wu et al., 2020).

The Slate Belt of the northern Central Range of Taiwan is a high-potential geothermal region comprised of tight host rocks (Fig. 1). The slate formations are with low primary porosity and impermeable if there are no natural open fractures (Liu et al., 2015; Song and Lu, 2019). The Jentse, Chinshui, and Tuchang areas are three important geothermal areas that have been explored for more than four decades in this region (e.g. Hsiao and Chiang, 1979; Tong et al., 2008; Tseng, 1978). Since the host rocks of the slate formations are tight, fault-related permeable structures or fractures related to regional stress field have been believed to be the main migration paths for geothermal fluid based on plenty of geological, geochemical and geophysical studies (Chang et al., 2014; Lu et al., 2017, 2020; Tong et al., 2008; Chiang et al., 2015). Over the past few decades, borehole imaging, such as fullbore formation microimager (FMI) logging, has often been used as an effective and efficient way to observe subsurface fractures (Barton and Zoback, 2002; Lai et al., 2018; Pöppelreiter et al., 2010). However, borehole images and other open-hole logging data are still limited in this region.

Because Jentse is a key geothermal prospect in the Slate Belt of the northern Central Range, the main objective of this study is using well log data to provide a detailed analysis of subsurface structures that includes the identification and characterization of fractures and fault zones, the evaluation of petrophysical properties of fault zones and host rocks, and the determination of hydraulic properties and possible factors controlling the development of permeable fault zones in Jentse. This study also aims to establish a workflow for the characterization of fault zones in Jentse and nearby geothermal areas. The workflow may also be helpful in future geothermal exploration and development in other areas with similar geological settings, such as structurally complicated or low-grade metamorphic areas.

2. Background

2.1. Regional geological setting

Taiwan is well-known as a site of active orogenesis caused by the northwestward movement of the Philippine Sea Plate and its collision with the Eurasian Plate (Shyu et al., 2005; Teng, 1996). The Philippine Sea Plate subducts beneath the Eurasian Plate, leading to the formation of the Ryuku Arc in Northern Taiwan. The Okinawa Trough, extending from southwestern Kyushu Island in Japan to the Ilan Plain, is a back-arc basin in the Ryuku Arc–Trench System (Fig. 1). To the south of the Ilan Plain, the northern Central Range has undergone a transition from a tectonic compressional regime to an extensional one (Teng, 1996). Earlier tectonic collisions had formed the high mountains and metamorphic host rocks. The later eastward extension of the Okinawa Trough has caused the regional extension and the development of the Ilan Plain (Lai et al., 2009). The latest extension that may just occur in the past million years in the southwestern part of the Okinawa Trough is characterized by normal faults with vertical to sub-vertical offsets that have existed since the Late Pleistocene (Shih et al., 2018; Shyu et al., 2005).

Abundant hot springs indicate the existence of high geothermal potential in the Ilan Plain and the northern Central Range (Liu et al., 2015). The primary heat source of the geothermal systems of the northern Central Range is believed to be the high-temperature metamorphic rocks in the rapidly uplifted mountain belts (Lin, 2000). Borehole data and
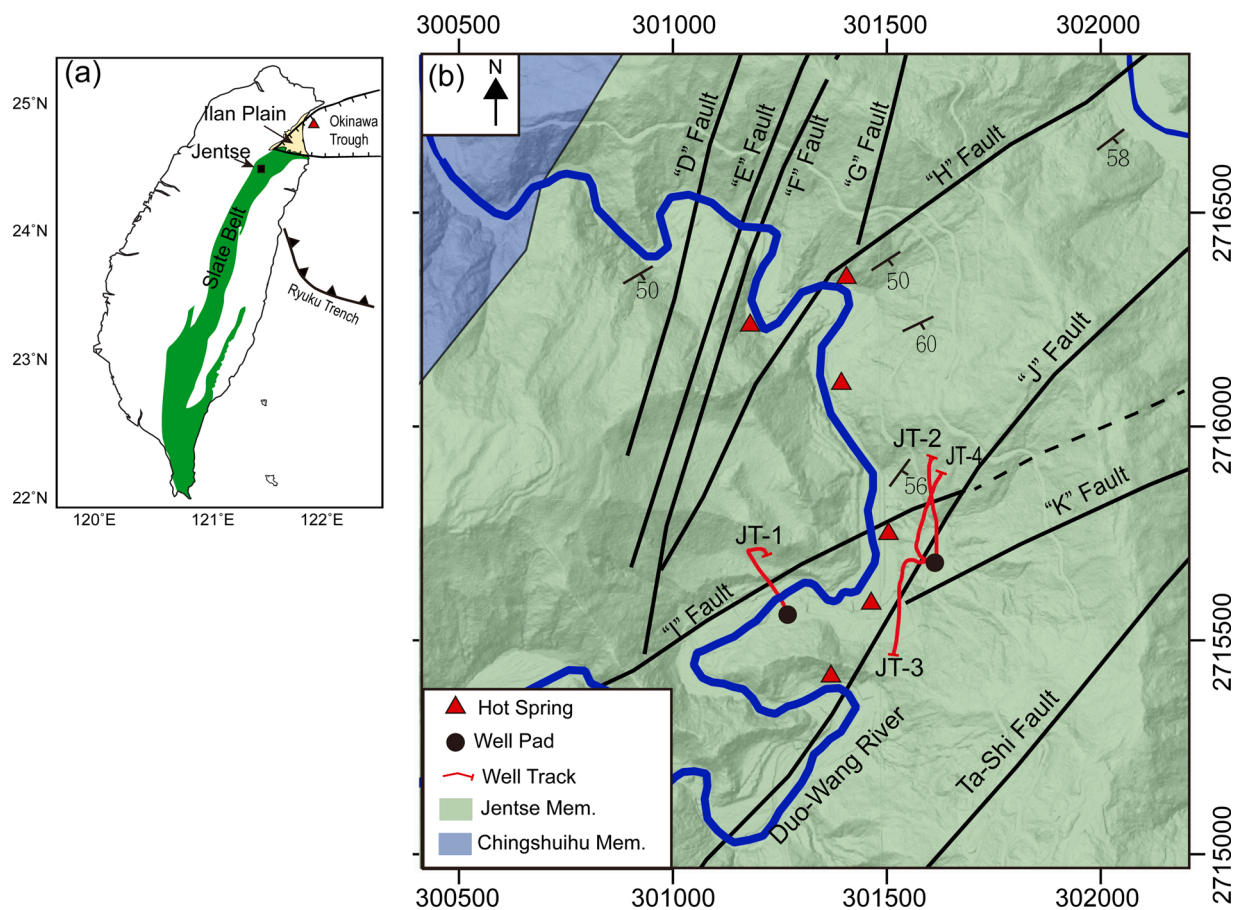

Fig. 1. (a) The study area, Jentse (black rectangular), is located in the northeast of the Slate Belt of the Central Range. The red triangular is the Turtle Island, (b) simplified geological map of the Jentse area (modified from Chang et al., 1986). (For interpretation of the references to colour in this figure legend, the reader is referred to the web version of this article.)

geochemical studies suggest that the temperature of the geothermal systems in northern Central Range is around 200–230 °C at depths of 2000–3000 m (Liu et al., 2015; Tong et al., 2008). Some geophysical and geochemical studies also suggest there may be a deeper magma-related heat source in this area (Lu et al., 2017; Tong et al., 2008).

The geothermal prospects, including Jentse, Chinshui, and Tuchang, in the northern Central Range, are all transected by faults. However, in this region, studies show that not all the faults and fractures are effective geothermal fluid conduits (Chang et al., 2014; Chiang et al., 2015; Lu et al., 2018, 2020; Tong et al., 2008). Lacking reliable subsurface data, it had been difficult to verify the subsurface hydraulic properties of faults. By new geothermal exploration well logging data, this study tried to reveal the characteristics of fault zones, which may lead us to better predict the location of permeable ones.

In Jentse, it is a series of NE-SW and N-E trending fault zones observed on the surface (Hisao and Tseng, 1979; Lin and Lin, 1995; Tseng, 1978). Some fault zones appear to be associated with the locations of some geothermal manifestations (Fig. 1). The widths of fault zones usually range from less than one meter to tens of meters on outcrops and only with minor offsets. Additionally, the orientations and extensions of these fault zones are difficult to be confirmed due to the poor continuities of outcrops. Since the scales and characteristics of the fault zones cannot be determined by surface observations alone, it is challenging to determine which fault zone on the surface is an effective geothermal migration path subsurface.

2.2. Regional stratigraphy and lithology

The stratigraphic unit exposed in the geothermal prospects of the northern Central Range is the Miocene Lushan Formation, which is mainly composed of slate (Lin and Lin, 1995). This Tertiary slate belt extends with a nearly N–S orientation for several hundred kilometers along the west flank of the Central Range (Fig. 1). The Lushan Formation is divided into the Kulu Member, the Chinshuihu Member, and the Jentse Member based on lithological differences (Hsiao and Chiang, 1979). The Jentse geothermal area is hosted by the Jentse Member. Compared to the other two members of the Lushan Formation, the Jentse Member contains higher portions of metasandstone, with the other two being mainly composed of slate. In Jentse, the exposed formations strike approximately NE-SW (N30–70 °E) and dip 30–90 °SE. Some steeply dipping or overturned beds are observed near faults.

The formations on the outcrops of the Jentse seem to have experienced a relatively low degree of metamorphism compared to other parts of the Lushan Formation (Chen et al., 2019). On outcrops, most of the bed boundaries of the formations and other features of sedimentary rocks have remained un-deformed, and cleavages are only poorly-developed. Since the low-grade metamorphic rocks were originally distal marine shale and sandstone, the occurrence of rocks exposed in Jentse is like those of interlayered tight shale and sandstone beds (Fig. 2). Therefore, the data properties of standard open-hole and FMI logs in Jentse would be similar to those in tight sandstone and shale.

2.3. Previous geothermal drilling in the Jentse area

Between 1974 and 1985, four geothermal exploration wells were drilled by the CPC Corporation, Taiwan (CPC), to depths of up to 2277 m in the Jentse area (wells JT-1 and JT-2) and the nearby Tuchang area (wells TC-8 and TC-9). The locations of these wells were mainly determined based on surface geological data (i.e., the locations of hot springs and interpretations of the orientation of the fault zones). The highest static formation temperature was 218 °C in well JT-2 at around 2000 m MD (CPC, 1984).

The existing spontaneous potential (SP) and electrical survey logs in wells JT-1 and JT-2 suggest that there may be permeable fracture zones passing through the boreholes at below 800 m MD in both wells (Lee and Lee, 1983; CPC, 1984). These putative fracture zones penetrated by the
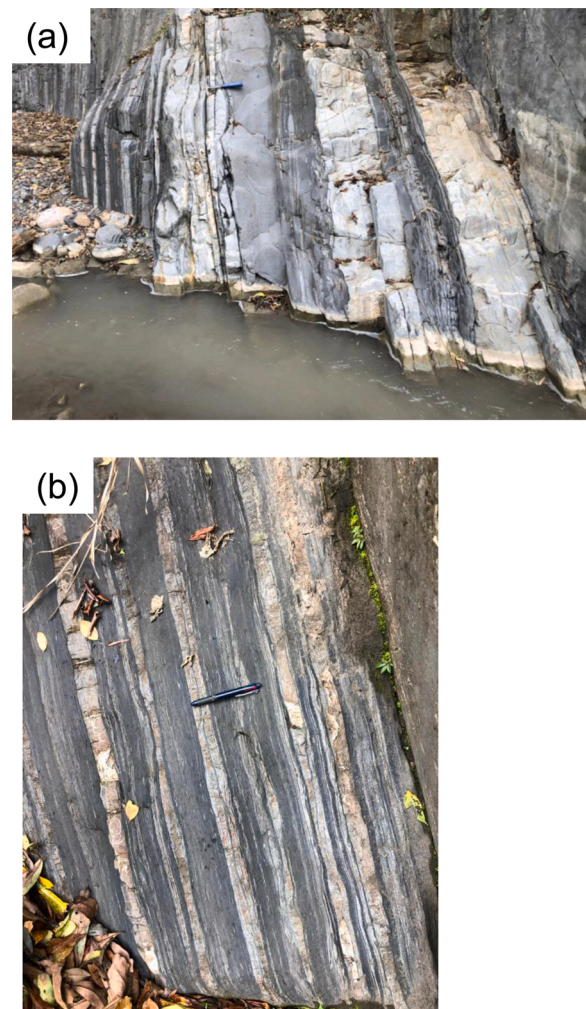

Fig. 2. Two outcrops locate by the Duo-Wang river close to the JT-3 well site at different scales. The outcrops show the lithology of metasandstone (bright color) interlayered with slate (dark color). In both (a) and (b), the bed boundaries are well-preserved, and cleavages are poor-developed.

wells are possibly associated with the fault zones observed in the outcrops near the drilling sites. However, the orientations and characteristics of the putative fracture zones had remained uncertain due to a lack of high-resolution continuous subsurface geological data.

From 2018–2019, CPC drilled two new geothermal exploration wells (wells JT-3 and JT-4) to depths of 1475 m MD and 1500 m MD in Jentse and encountered bottom-hole temperatures of 180 and 205 °C, respectively. These wells targeted permeable fracture zones and/or fault zones at approximately 800–1500 m MD. Wells JT-2, JT-3, and JT-4 were drilled in the same well pad as it is difficult to find flat surfaces for drilling. In this study, the newly acquired standard open-hole and FMI logs in well JT-3 were used to characterize the subsurface permeable fracture structures.

3. Data and workflow

3.1. Log data of well JT-3

This study uses well log data acquired from well JT-3 to reveal the characteristics of subsurface structural features such as faults and fractures. Well JT-3 is a directional well that deviates toward the south. From 200–800 m MD, the borehole inclination is about 2–12° toward the south, while from 800 to 1475 m MD (8.5-inch-diameter interval), the borehole inclination is about 10–22° toward the same direction. The

temperature log used in this study was conducted under a static condition that the well had been full shut-in 271 days after drilling. The static formation temperature is about 160–180 °C in the 8.5-inch-diameter interval. A four-day short-term flow test using the James lip pressure method was conducted in the JT-3 well. By using a four-inch pipeline, the final production rate of the well was 48 t/h at 3.3 bar-g wellhead pressure with 138℃ wellhead temperature.

Well JT-3 was logged from 10 m MD to the borehole bottom using Schlumberger© integrated wireline logging tools. The studied well interval was from 800 to 1475 m MD in the 8.5-inch-diameter well section. The logs analyzed included standard open-hole and FMI logs. The standard-open hole logs included Caliper (CAL), Gamma Ray (GR), Deep Resistivity (RT), Neutron Porosity (NPHI), Bulk Density (RHOB), and Sonic Slowness (DT) logs (Fig. 3). Compared to the one-dimensional values of standard open-hole logs, FMI logs provide electrical images of borehole surfaces to delineate the lithological and structural features on them. It is the most efficient way to observe fractures continuously in boreholes to date. Additionally, drill cuttings (collected in a 10 m interval), the temperature log, and 5-m-long cores (839–841 m MD and 978–981 m MD) of the JT-3 well were also used to examine the log interpretation results in this study.

3.2. The workflow of standard open-hole log data analysis and interpretations

3.2.1. Quality checks and preliminary editing for the standard open-hole logs

The apertures of subsurface fracture planes are commonly at the millimeter scale; therefore, the resolution of standard open-hole logs often precludes the detection of a single fracture plane (Crain, 2013). However, in real geological cases, open-hole logs often respond to the development of fracture zones (Hamahashi et al., 2015; Jeppson et al., 2010; Lyu et al., 2017).

The standard open-hole and FMI logs were processed and analyzed using the Schlumberger Techlog Software Platform. The standard open-hole logs were first examined, after which the procedures of depth matching among each log and the removal of abnormal or spiky log values were conducted. Abnormal or spiky log values are the readings not in the general log response ranges of rocks and minerals. For example, the rock density values that are less than 1.0 g/cm3 or the sonic slowness value that are larger than 240 us/ft. These abnormal readings usually exist as singular points and made the log curves spiky. Such values were usually caused by electrical or mechanical engineering issues during surveying.

The examination of the CAL log data showed that some intervals between 800–950 m MD were washed out and caused the poor qualities of the RHOB and NPHI logs (Fig. 3). Consequently, these two logs had to be reconstructed before interpretation. The qualities of other logs in this interval and all open-hole logs between 950–1475 m MD were sufficient for interpretation after basic editing.

We applied the multi-linear regression function of Techlog and the log curves below 950 m MD to reconstruct reliable NPHI and RHOB logs for the washed-out interval. After the reconstruction and basic data editing, the quality of the open-hole logs of all of the studied intervals was good enough to conduct petrophysical and fracture analyses.

3.2.2. Shale volume (Vsh) calculation and lithological interpretation

Since the occurrence of the siliceous slate and metasandstone in Jentse is similar to those of tight siliceous shale and sandstone, this study used the log interpretation workflow for siliceous sedimentary rocks to conduct open-hole log interpretations. The procedures included shale volume (Vsh) calculations, lithological interpretations, and effective porosity (PHIE) calculations (Crain, 2013). Since there are no hydrocarbons in this area, the water saturation was assigned to be one.

The comparisons among GR, NPHI, and RHOB logs showed how these logs responded to the compositions of slate and metasandstone. On

the crossplot, the RHOB and NPHI log values were mainly on the linear trend between two endpoints representing tight pure metasandstone and tight pure slate, respectively (Fig. 4). The tight metasandstone usually showed low GR, low RHOB, and low NPHI log values, and slate showed high GR, high RHOB, and high NPHI log values. Since the fractured rocks had lower density and higher water contents in fractures, both the fractured metasandstone and slate would both have higher RHOB and NPHI log values comparing to their un-fractured counterparts.

Similar to which of the fractured rocks with free water, hydrothermal alterations may produce clay minerals with bound water, causing the rocks to be high NPHI, low RHOB, high DT, and low RT readings (Crain, 2013). In this situation, the GR log and the lithology observations of cuttings would be beneficial to distinguish clay-rich geo-thermally-altered rocks (high GR) and fractured rocks (low GR).

The gamma-ray radiation levels of fractured rocks did not change compared to the intact ones, so the GR log values did not change due to fracturing. Therefore, this study used the GR logs to calculate Vsh and to construct the lithological column via Eq. (1) from Crain, 2013. Vsh represents the shale fraction of a unit rock volume and can be calculated using the following equation:

$$Vsh = \frac{GRlog - GRmin}{GRmax - GRmin} \tag{1}$$

where Vsh is the volume of shale (v/v), GRlog is the GR log reading (unit: API), GRmin is the GR of pure metasandstone (API), and GRmax is the GR of pure slate (API).

3.2.3. Effective porosity log (PHIE) calculations

According to the porosity measurements conducted in core samples of 980 and 981 m MD, the effective porosity of the matrix of slate was less than 0.01. However, the development of fractures may increase the porosity-log values due to the increase in empty spaces for fluids. This study used the effective porosity log (PHIE) as an indicator of open fractures in open-hole logs. Although several kinds of open-hole logs in this study, such as RHOB, DT, and RT, reflected the development of fractures visually, however, the fracture responses on these logs were masked by lithological variations to varying degrees. We believe the calculated PHIE log would effectively reduce the weightings of shale or clay minerals in the response of open-hole logs. The PHIE log was calculated using Eq. (2) to (5) according to Crain (2013):

$$PHIE = \frac{PHIEn + PHIEd}{2} \tag{2}$$

where PHIEn (v/v) is the effective porosity derived from NPHI, and PHIEd (v/v) is the effective porosity derived from RHOB. PHIEn and PHIEd logs were derived from Eqs. (3) and (4):

$$PHIEn = NHPIlog-Vsh*PHINSH \tag{3}$$

$$PHIEd = PHID-Vsh*PHIDSH \tag{4}$$

where NHPIlog (v/v) is the NPHI log reading, PHINSH (v/v) is the NPHI of pure slate, PHIDSH (v/v) is the total neutron porosity of pure slate derived from RHOB, and PHID (v/v) is the total density porosity derived from RHOB log reading. PHID was calculated from RHOB by Eq. (5):

$$PHID = \frac{RHOBma - RHOBlog}{RHOBlog - RHOBfl} \tag{5}$$

where RHOBma (g/cm^3) is the RHOB of pure metasandstone, RHOBlog (g/cm^3) is the RHOB log reading, and RHOBfl (g/cm^3) is the RHOB of pure formation fluid.

3.3. Interpretation of the FMI logs

Targeting suitable drilling prospects in structure-controlled geothermal areas remains challenging due to the difficulties in
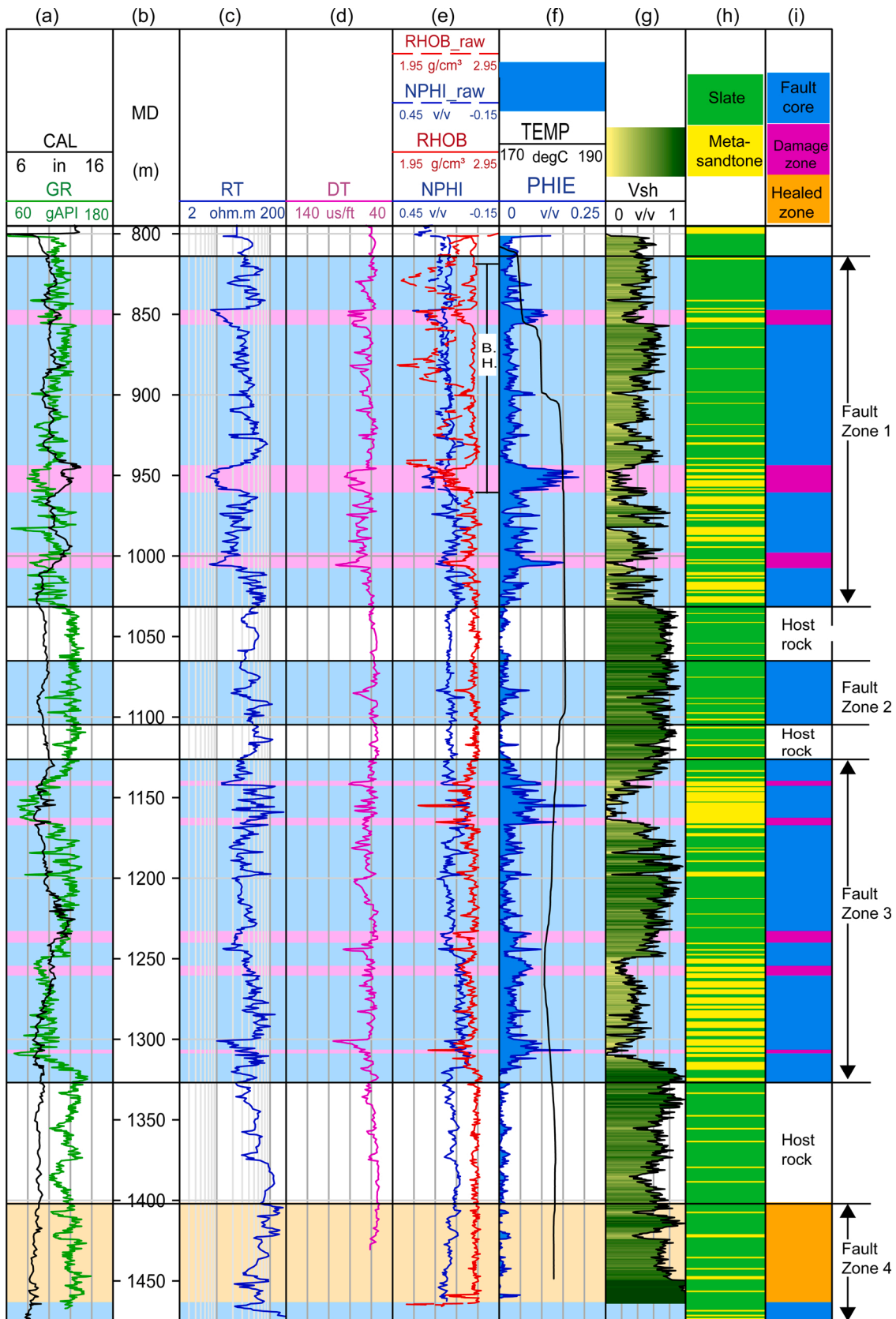
Fig. 3. The open-hole logs used in this study and interpreted logs (CAL: Caliper; MD: measured depth; GR: Gamma Ray; RT: Deep Resistivity; DT: Sonic Slowness; RHOB: Bulk Density after reconstructed; NPHI: Neutron Porosity after reconstructed; PHIE: Effective porosity; TEMP: Borehole Temperature; VSH: Shale Volume). The RHOB and NPHI logs of 800-950 m MD before rebuilt were RHOB_raw and NPHI_raw logs. The depth column (b) is shown in measured depth (MD). The column (h) is the lithology interpreted by the cuttings description, and the column (i) is the zonations interpreted by the open-hole and FMI logs. B.H. in column (e) is the bad hole interval.
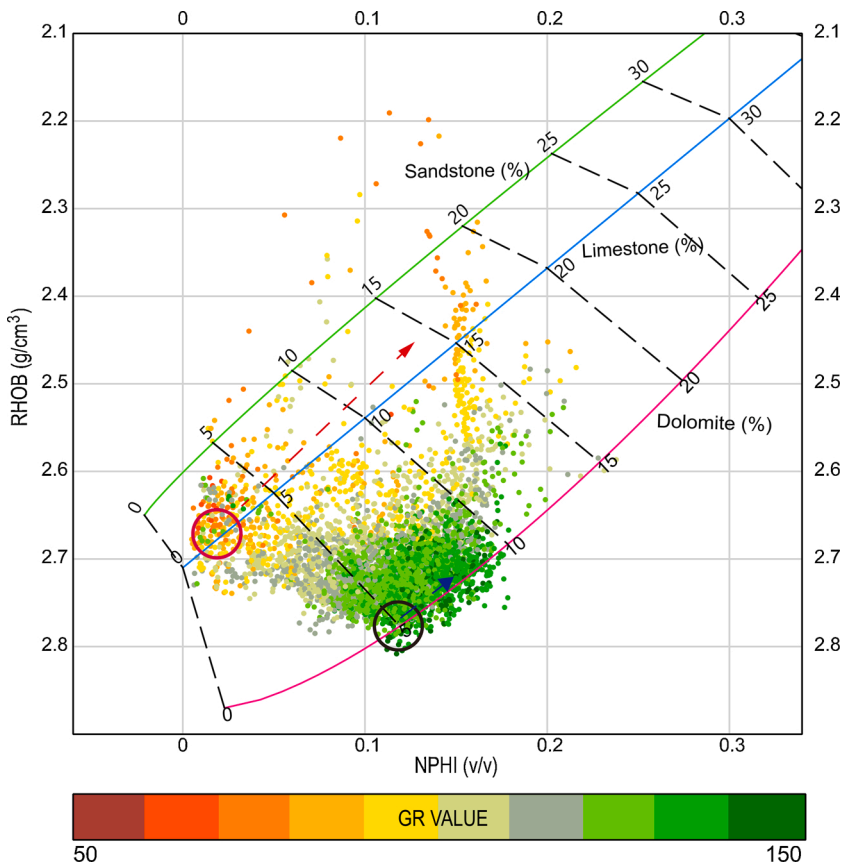
Fig. 4. Lithological identification by crossplot of NPHI and RHOB with GR in color. Red and black circles show the values of tight metasandstone and tight slate respectively. The values of tight rocks are in the linear trend between the two circles. The RHOB and NPHI values of fractured metasandstone and slate shift from the linear trend along the direction of the red and blue arrows in the figure. (For interpretation of the references to colour in this figure legend, the reader is referred to the web version of this article.)

characterizing subsurface structures in terms of their hydraulic behaviors. Measurement sensitivity in combination with approximately 80% circumferential coverage (in an 8.5-inch-diameter wellbore) makes FMI images useful for identifying subsurface structures and providing direct data on in-situ stress orientations (Pöppelreiter et al., 2010; Barton and Zoback, 2002; Schlumberger, 2015). Accurate high-resolution FMI images enable fractures and faults to be characterized as open or sealed (Ameen, 2014; Schlumberger, 2015). Knowledge of the depths and orientations of permeable structures is beneficial to the study of both around boreholes and in the regional reservoir scale. An improved understanding of the distributions and properties of permeable fractures can allow the optimization of operations and the improvement of decisions regarding future well targets in geothermal exploration or development projects.

3.3.1. Raw data processing and the data quality of FMI

To generate FMI images for interpretation, the raw FMI log data were processed in Techlog. After procedures of inclinometry testing, depth matching, image equalization, and image normalization, the processed static and dynamic images displayed plane features of bed boundaries and natural fractures as sine-curves except for a few short intervals that were affected by bad borehole conditions. The quality of the processed FMI image was suitable for fracture analysis and interpretations.

3.3.2. Interpretations of the FMI images

In the processed FMI images of this study, the penetrated formations are composed of interbedded metasandstone and slate and their bed boundaries could be easily identified. Therefore, this study used bed boundaries as key reference features in the interpretation of FMI images. As faulting or shearing sometimes rotated formation beds abruptly, drastic rotations of beds often indicate faulting. To locate the positions of faulting, we picked bed boundaries every 1–2 m and observed changes in bed orientations (Fig. 5). Additionally, systematic bed

rotations over a long span of the well interval were also used as an indicator of larger-scale structural features.

In addition to bed boundaries, natural fracture planes and breccia zones were also common features in the FMI images. Natural fracture planes could be divided into natural open and sealed fractures. Natural open fractures appeared as dark-colored sine-curves in FMI images due to the infiltration of low-resistivity water-based drilling mud. Meanwhile, sealed fractures often appeared as bright-colored sine-curves due to the response of high-resistivity mineral cement in the fractures. Low-resistivity minerals, mainly clay minerals, precipitated within fractures may also cause dark-colored sine curves in FMI images. By open-hole logging data and cutting descriptions, this study suggests there were rare clay minerals within fractures. Therefore, this study treats all dark-colored fractures as natural open fractures. The detailed reason would be explained in Section 5.4. And then open and sealed fractures would also be subdivided into different types of fractures based on their characteristics, which is demonstrated in Section 4.2.2.

The most common drilling-related features are drilling-induced tensile fractures and borehole breakouts. These features can indicate the direction of the stress field. Drilling-induced tensile fractures usually extend parallel to the direction of maximum horizontal stress. In contrast, the extension direction of borehole breakouts is usually parallel to the direction of minimum horizontal stress. In this study, bed boundaries, natural fractures, and drilling-related features were identified and analyzed in terms of their positions, orientations, and characteristics.

3.3.3. Computation of fracture density, fracture aperture, and fracture porosity

Via the picked fractures, this study calculated 1) the number of fractures per meter, also known as "fracture density," 2) apertures of fracture planes also known as "fracture aperture," and 3) volume within the apertures of fracture planes per unit borehole volume, also known as
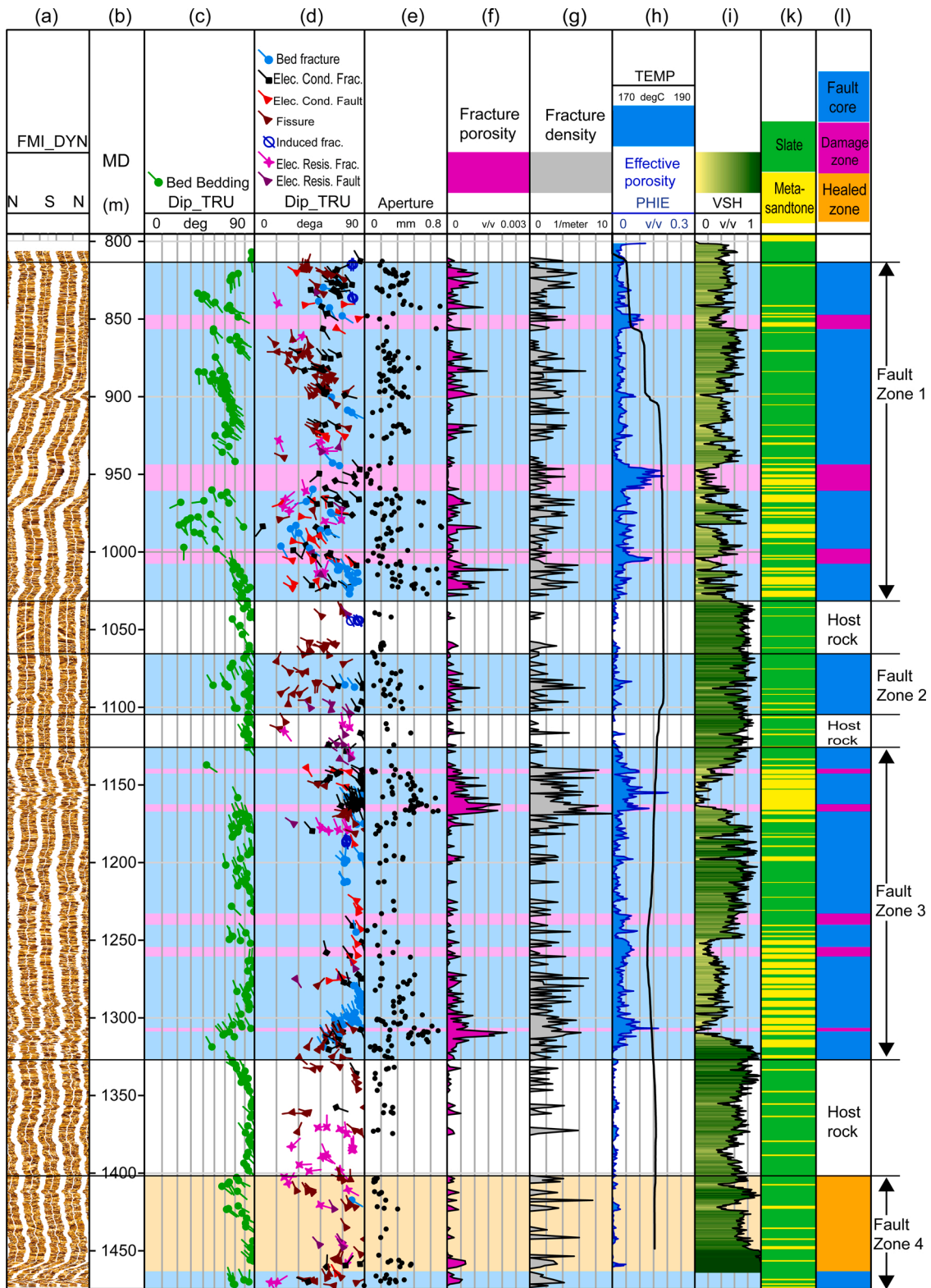
Fig. 5. The interpretation of the FMI images (columns (c) – (g), and (l)) and the comparisons to the borehole temperature (TEMP), effective porosity (PHIE), and lithology.

"fracture porosity." These parameters are commonly used to indicate the productivity of fractures or fractured zones (Ameen, 2014; Crain, 2013; Schlumberger, 2015).

In this study, the numbers of fracture planes were counted in a one-meter sliding window. The fracture density was the average number of fractures in one-meter window length which had been corrected via the relations between fracture orientations and borehole orientation by the Terzaghi correction method (Terzaghi, 1965). This correction is not reliable for fractures that are nearly parallel to the borehole because the numbers of intersections between fractures and the borehole would be highly biased (Priest, 1993; Schlumberger, 2015). In this study, the maximum angle between the poles to the fractures and the borehole was

set at 85˚.

Fracture apertures were calculated by the method proposed by Luthi and Souhaite in Techlog (Luthi and Souhaite, 1990; Schlumberger, 2015). By this method, the value should be reliable when the calculated apertures are between $10\,\mu m - 1\,mm$; however, the calculated values may be smaller than actual numbers when the true apertures of fractures are larger than 1 mm (B. Liu, personal communication, September 14, 2020). Besides, the possible effects of electrically conductive minerals precipitated within fractures are also required to be considered according to different geological settings. Based on the results of the fracture apertures, fracture porosity was also calculated. These parameters of fractures were output as continuous curves in this study.

3.4. Fracture zoning based on fracture characteristics

According to the FMI images, we found that fractures were not evenly distributed. Some intervals featured a high density of fractures while other intervals were almost intact. Additionally, fractures could also be characterized by rock-fragment-dominated intervals, open-fracture-dominated intervals, and sealed-fracture-dominated intervals. Therefore, we separated fractures into different zones based on their densities and characteristics for further interpretations and discussions.

4. Results

4.1. The results of open-hole log interpretations

4.1.1. Vsh and lithological interpretations of open-hole logs

The GR log values of the studied well section are mainly between 50 and 150 API. Based on the ranges of GR values, we used Eq. (1) to generate the Vsh log (Fig. 3). According to the calculated Vsh, the formations were separated into three rock types—namely 1) metasandstone ($0 \leq Vsh \leq 0.3$), 2) sandy slate ($0.3 < Vsh \leq 0.7$), and 3) slate ($0.7 < Vsh \leq 1$). By comparing the Vsh log with the lithology interpretations of drill cuttings and cores, this study confirmed that the Vsh log by GR log is a reliable indicator of lithology.

4.1.2. The PHIE log and its characteristics

After generating the Vsh log, we used the NPHI, RHOB, and Vsh logs to calculate the PHIE log. The results showed that the PHIE values are less than 0.05 in some intervals, such as 1100–1300 m MD, regardless of the rock types. Such low values are reasonable for both tight metasandstone and slate in this region. However, in some other intervals, such as 800–1000 m MD, the calculated PHIE values were higher than 0.05, and sometimes even higher than 0.1 in some shorter intervals (Fig. 3). These high values are the result of rock fracturing. The developments of fractures were also verified by the interpretation of FMI images. In this study, we used the PHIE log instead of neutron porosity to find the possible location of porous fractured intervals because the PHIE log would reduce the possible pore-like response from the possible precipitated clay minerals in fractures. This method is a common practice in the oil and gas industry (Crain, 2013). Besides, in the interpreted fractured zones with high PHIE, we could find the GR readings are low and the rock type is mainly metasandstone (Fig. 3). This proves the high NPHI, low RHOB, and low RT indicating porous fractured intervals but not clay-rich intervals.

4.2. The results of interpreting the FMI images

4.2.1. Orientations of formation beds

The studied well interval showed clear interlayering of metasandstone/slate in the FMI images. According to the picked orientations of bed boundaries, we found that most formation beds changed smoothly and gradually in sequence. In some short intervals, the beds displaced rapidly but progressively showed in dip and dip azimuth angles (e.g. 825–840, 1080–1087 m, and 1310–1330 m MD) showed in Fig. 5(d).

Such abrupt changes in bedding angles are often associated with local faulting. Even though folding would also generate fracture systems (Watkins et al., 2018); however, in Jentse, folds are only developed with large fault zones and often in minor scales. Therefore, this study interprets faulting should be the major mechanism to form open fractures. This faulting interpreted by the orientation of beds would be verified by the interpretations of fracture features by the FMI images.

In addition to the abrupt changes in the orientation of bed boundaries, there were also apparent rotations in the general trends of the attitudes of the formations (Fig. 6). The trends are as follows:

1) N40°–50 °E / 40°–80 °SE (800–930 m MD);
2) N50°–70 °E / 60°–90 °SE (1000–1040 m MD);
3) N60°–70 °E / 60–90 °NW (1040–1350 m MD); and
4) N40°–50 °E / 40°–80 °SE (1350–1475 m MD).

Compared to the regional orientations of formations, the formations between 1040–1350 m MD were rotated to dipping toward the SE direction. The rotation of formations reflected the major structural/tectonic trends in the area, which are discussed in Section 5.2.

4.2.2. Fracture type, morphology, and orientation

Regarding natural fracture planes, four types of natural open fractures and two types of natural sealed fractures were observed in this study (Fig. 7). In addition to the features of fracture planes, there were also several dark-colored breccia zones consisting of rock fragments observed in the studied well section. With the correlation to petrophysical logs, we found dark-colored fractured intervals have high PHIE and low GR values. It implies most of the dark-colored fractures and brecciated zones should be porous but not clay-rich. The four types of natural open fracture planes include bedding fractures, electrically-conductive fractures, electrically-conductive faults, and fissures. These four types of natural fracture planes all appeared as dark-colored sine curves in the FMI images.

Most of the electrically-conductive fractures strike parallel to their adjacent formation beds but dip toward the opposite directions of the dip of the adjacent formation beds (Fig. 8). Bedding fractures were developed on bed boundaries; however, it is not difficult to differentiate bedding fractures from the features of bedding boundaries. The bedding fractures were usually wider and had more irregular or distorted surfaces than bedding boundaries. Electrically-conductive faults showed clear offsets between the two sides of the fault planes, and there were no distinct offsets between the two sides of the fracture planes. Fissures show poorer continuities and weaker color contrasts to the background rock matrix than the other types of natural open fractures.

The two types of natural sealed fractures are electrically-resistive fractures and electrically-resistive faults; they all appear as bright-colored sine curves in the FMI images. Sealed fractures are much thinner and more unclear than open fractures in the FMI images. Additionally, the orientations of sealed fractures are more scattered than those of natural open fractures. Electrically-resistive faults show clear offsets between the two sides of the fault planes, however, electrically-resistive fractures do not.

These six types of natural fractures, including open and sealed ones, all have a dominant strike of NE-SW and mainly dip toward the NW or SE at high angles (Fig. 8).

Drilling-induced tensile fractures appeared as near-vertical, dark-colored straight lines striking NE-SW. Compared to drilling-induced tensile fractures, borehole breakouts were rare and unclear within the studied intervals, and therefore this study did not use borehole breakouts for further geological interpretations.

4.2.3. Statistics of fracture density, fracture aperture, and fracture porosity

Statistical analyses of fracture parameters were conducted on the selected natural open fractures, the fracture density varied from 0 to 10 trace/m. The fracture aperture ranged from 0 to 0.75 mm, and the
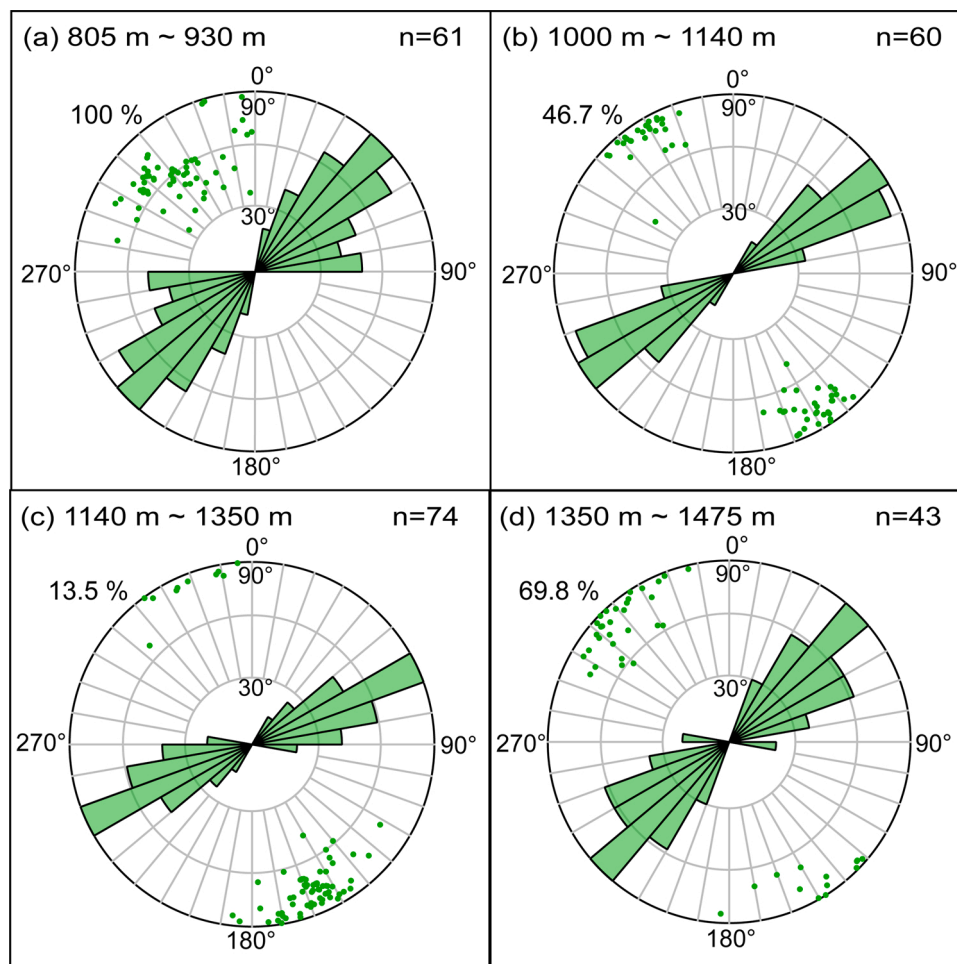
Fig. 6. Orientations of bed boundaries. The number of n shows the numbers of bed boundaries picked in the defined interval. The percentage in the upper left of the individual plot is the percentage of bed boundaries dipping toward the SW. From (a) to (d), the dominant dip direction is from toward the SE toward the SW and then back toward the SE.

fracture porosity ranged from 0 to 0.0022 (Fig. 7).

4.3. Zonation based on fracture characteristics

According to the orientation changes and fracture development observed in the FMI images, this study found that fracture structures, such as natural open fracture planes and fault breccia, are unevenly clustered within the studied well section. Such highly fractured zones may be indicators of the positions of fault zones, so this study defined fault zones based on the following criteria:

1) the values of fracture density, fracture aperture, and fracture porosity,
2) the occurrence of breccia zones or fracture plane cluster zones,
3) abrupt changes in bed orientations (either magnitude or azimuth).

A total of four fault zones were identified in the FMI images, and each fault zone was separated by intact host rock zones (Fig. 5). Within the four fault zones, we also recognized the characteristics of different internal structures of fault zones. Breccia zones are porous fault cores, the open fracture cluster zones are fault damage zones next to fault cores, and the sealed fracture cluster zones are healed zones within fault zones (Fig. 9). In this studied well section, there is only one healed zone, located in Fault Zone 4, identified (Figs. 3 and 5).

According to the zoning criteria and characteristics of fault cores and damage zones, Fault Zone 1 (800–1030 m MD) is composed of three

fault cores and four fault damage zones. Fault Zone 2 (1060–1110 m MD) is comprised of only a single fault damage zone. Fault Zone 3 (1125–1325 m MD) is composed of five thin fault cores and six fault damage zones. Fault Zone 4 (1400–1450 m MD) is composed of one healed zone and one damage zone.

5. Discussion

5.1. Characteristics of the fault system

5.1.1. The characteristics of fault zones and internal structures

In this studied well section, this study identified four fault zones (Fault Zones 1–4) separated by intact host rocks. Since Fault Zones 1–3 are spatially close and share similar fracture features, this study regarded these three fault zones as comprising a major permeable fault system. We believe that the lower part of Fault Zone 1 from 940 to 1030 m MD may be the most permeable interval within the fault system due to the development of two thick porous fault core and adjacent damage zones (Fig. 5).

The healed zone of Fault Zone 4 is composed of mainly sealed fractures and small numbers of open fractures. Even though calcite and quartz are the most common minerals within sealed fractures of the slate belt (Lu et al., 2018; Song and Lu, 2019), this study does not observe high contents of calcite veins or quartz veins in cuttings within the Fault Zone 4 comparing to other intervals. The possible reason for the low calcite or quartz contents may be the original apertures of the fractures
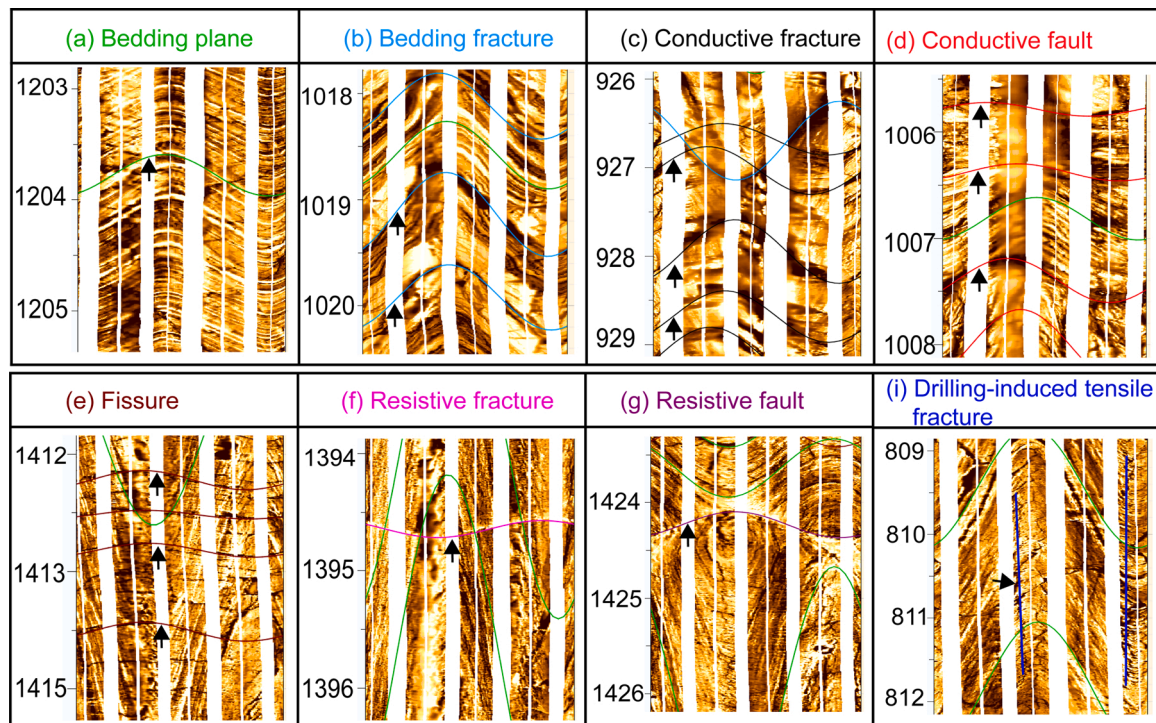
Fig. 7. Subfigure (a) shows the typical features of bed boundaries in the dynamic FMI image. The subfigures (b)-(i) show different types of fracture planes. The black arrows mark the mentioned features in each subfigure. The number in the right is the measured depth in the meter scale.

in Fault Zone 4 were small. Therefore, the total volumes of the later precipitated minerals might not be not abundant. Due to the development of the healed zone, this study considers Fault Zone 4 relatively inactive comparing to Fault Zones 1–3; however, the timing of its faulting period was not clear due to lacking age data.

The low quantities of calcite and quartz could also be validated by the high GR response of Fault Zone 4 indicating the main compositions are clay minerals in slates with higher radioactivity than quartz and calcite. Because Fault Zone 4 has a similar average petrophysical response to the host rock (Fig. 3), such as low effective porosity, low fracture porosity, and stable caliper size, we suggest it is not that permeable comparing Fault Zone 1–3. However, the quantitative differences of permeability between them are remained unclear due to lacking the flowing data.

In this study, the average fracture densities and average fracture porosities of the fault core zones are lower than that of the damaged zones (Fig. 10). The reason is that we did not pick a large number of fracture planes in the fault cores since they were actually composed of breccia but not fracture planes. However, according to the high PHIE values within them, the fault cores should be the most permeable zones in the studied well interval.

5.1.2. The correlations among lithologic log, temperature log, and internal structures of fault zones

To confirm the flow properties interpreted by the open-hole logs and the FMI log, we correlate the fault zones to static borehole temperature and lithologic logs. The lithologic log interpreted by cuttings is consistent with the Vsh log which also implies the possible lithology (Fig. 3). Besides, it could be found the fault cores often developed in metasandstone beds, and intact host rock zones usually developed in thick slate beds. The relations between lithology and faulting would be further discussed in Section 5.2.1. In cuttings, this study found there are rare calcite, quartz veins, and clay minerals that might be formed by hydrothermal alteration in the whole studied well section. This finding is also consistent with that there are few sealed-fractures found in the FMI log.

This study used the static borehole temperature log measured 271 days after drilling to correlate with the fault zone structures. Although there is a minor depth shift, we could observe the temperature increased about 4 ℃ at the first fault core of Fault Zone 1. Then, the temperature remains high from the lower half part of Fault Zone 1 to the bottom of Fault Zone2. There is a 2 ℃ temperature drop at the bottom of Fault Zone 2. Then, the temperature becomes lower in Fault Zone 3, and the lowest part is located at the major fault cores of Fault zone 3. From the Bottom of Fault zone 3, the temperature remains stable and becomes lower gradually toward the well bottom indicating the Fault Zone 4 is less permeable than Fault Zone 1–3. The variations of temperature log confirm the permeable fault zone structures identified by FMI logs should be correct.

5.2. The controlling factors of fracture characteristics within the fault system

The study results showed the characteristics of the fracture within the fault system are controlled by lithology, fault displacement, fault activity, and the direction of principal horizontal stress. The detailed relationships among these properties and the fault system would be discussed in this section.

5.2.1. Lithology

The fault cores observed in the studied well interval were all composed of brecciated rock fragments but not fault gauges, and mainly located within metasandstones beds (Fig. 5). It is widely accepted lithology would be a major factor that controls the degree of faulting, mitigated by the degree of compression or tension within the fault plain (Bense et al., 2013; Sibson, 1996). Brittle rock with higher tensile strength, such as metasandstones in this study, fails (breaks) under strain and thus would have greater potential for higher permeability (Wallis et al., 2012). Slates that are with high phyllosilicate mineral content, tend to undergo plastic deformation and shearing rather than breakage. Plastic deformation of these softer rocks will usually have very low permeability. Therefore, when fault zones penetrate metasandstone
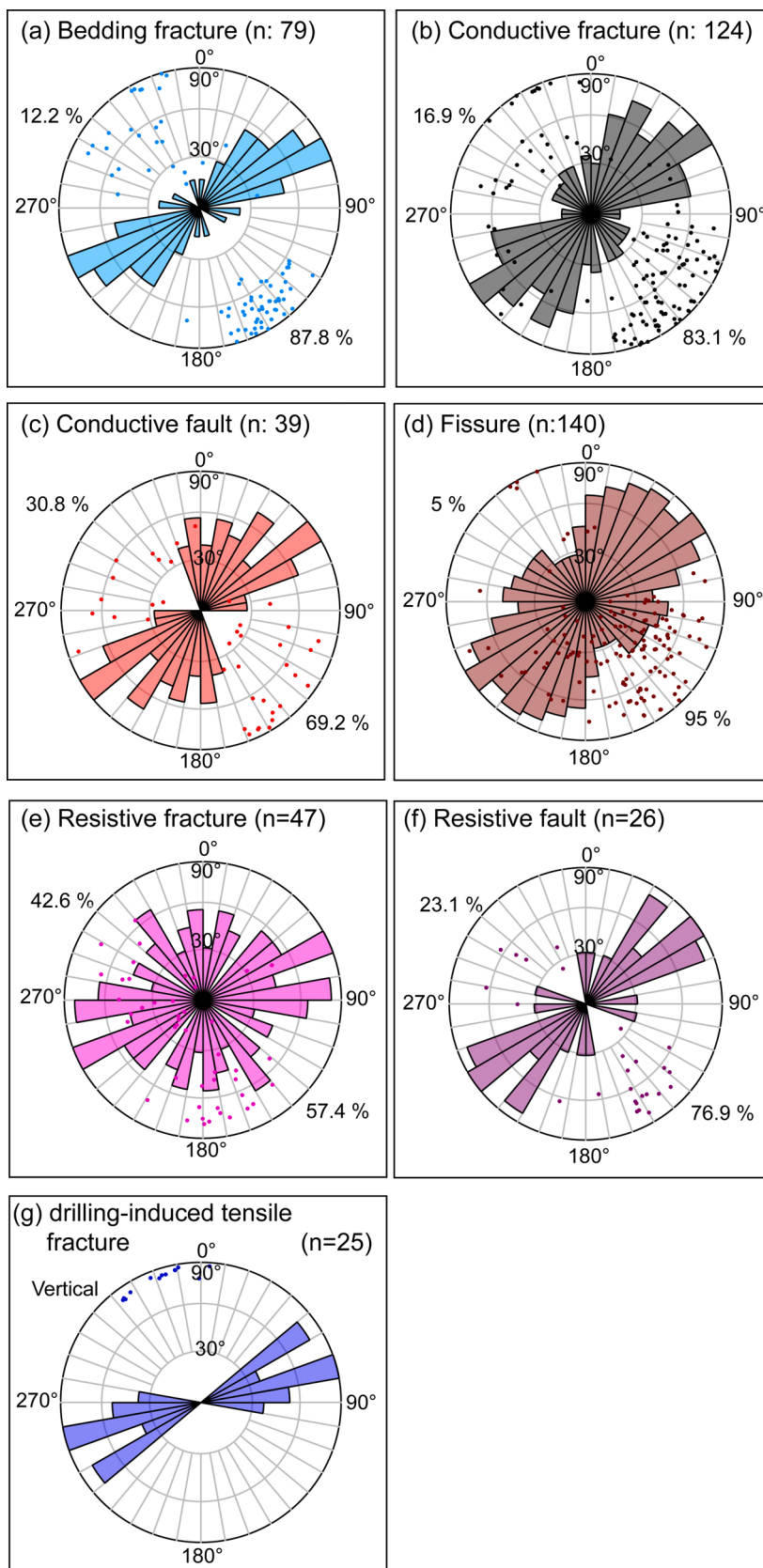
Fig. 8. Orientations of different types of fracture planes. The number of n shows the numbers of fractures picked in the studied well interval. The percentage in the upper left of the individual plot is the percentage of fractures dipping toward SW.
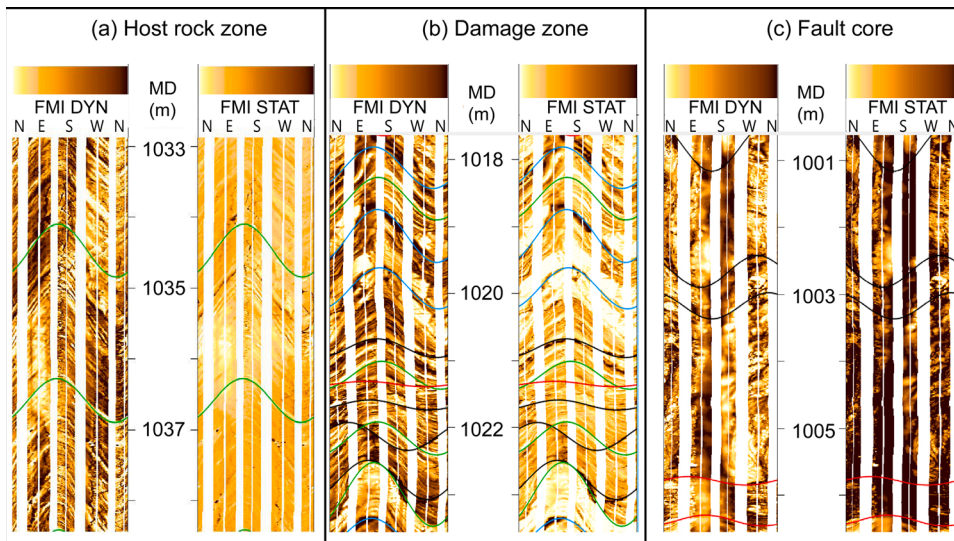
Fig. 9. FMI images of the typical intact host rock, fault damage zone, and fault core. Green curve: bad boundary; light blue curve: bedding fracture; black curve: electrically-conductive fracture; red curve: electrically-conductive fault. In fault core (c), angular-subangular rock fragments (bright color spots) are surrounded by dark-colored drilling mud observed in the dynamic FMI (FMI_DYN) image. (For interpretation of the references to colour in this figure legend, the reader is referred to the web version of this article.)
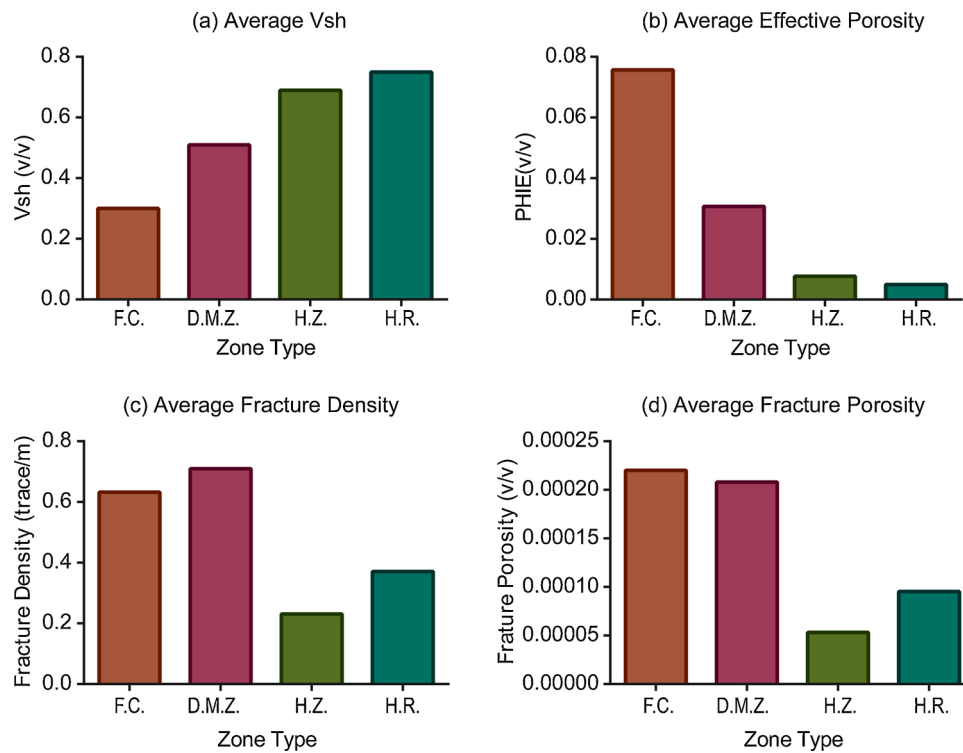

Fig. 10. The average Vsh, effective porosity, fracture density, and fracture porosity of different types of zones, which are the fault cores (F.C.), the fault damage zones (D.M.Z.), the host rock (H.R.), and the healed zone (H.Z.).

beds, the rocks are easier to be broken and brecciated (Fig. 10). On the contrary, when fault zones penetrate the sandy slate and slate beds, the rocks more easily develop shearing deformation. For example, where Fault Zone 1 penetrates the metasandstone interval between 943.6–960.6 m MD, the rock is highly fractured and has developed brecciated fault cores (Fig. 5). Within Fault Zone 2, the slate interval between 1065.2–1105 m MD has a lower magnitude of fracturing compared to the sandy slate intervals in Fault Zone 1 or Fault Zone 3.

5.2.2. Fault displacement

In Section 5.2.1, we mentioned the importance of lithology on the mechanisms of faulting. In addition, fault displacement may be another important factor controlling the development of internal structures of

fault zones. In the studied well intervals, the dark-colored fault cores with bright-colored rock fragments are mainly low GR, low RT, and high PHIE indicating the cores should consist of porous fault breccia but not clay-rich fault gauges. However, large fault displacements may eventually cause the permeable fault breccia to be non-permeable fault gouges (Gray et al., 2005; Holland et al., 2006; Micarelli et al., 2006). Therefore, we consider the smaller fault displacements that could generate fault breccia but not fault gouges in fault cores would be better for geothermal production. The small fault displacement may be one of the reasons that Fault Zone 1–3 are permeable ones.

5.2.3. Fault activity

The regular faultings is a key to keep the fractures open within the

fault system. If the activity of faults slows or stops, the porous spaces within brecciated zones and the apertures of fracture planes may gradually close up or become fully filled by later mineral cementation (Zoback, 2007). The healed zone of Fault Zone 4 is a good example of a non-permeable fault zone in the study area. Since most of the fractures have been cemented and the values of PHIE are as low as those of intact host rocks in Fault Zone 4, we believe that the permeability of healed faults should be as low as that of the intact tight host rocks in this region. The static borehole temperature log also shows the Fault Zone 4 is less promising that Fault zone 1–3 (Fig. 3).

5.2.4. Direction of principal horizontal stress by the FMI log

Generally, in vertical to near-vertical wells, the strike of drilling-induced tensile fractures is aligned with that of the maximum horizontal stress. However, this may not be the case for a deviated well section like the well section we studied (Peška and Zoback, 1995). Hence, we checked the strike of the drilling-induced tensile fractures that were developed in shallow vertical well intervals of well JT-3. The strikes of the drilling-induced tensile fractures were found to be NE-SW, which is similar to those of the 800–1475 m MD well section. Therefore, according to the consistent NE-SW-striking drilling-induced tensile fractures in different well sections, the direction of maximum principal horizontal stress should be also NE-SW. The direction of maximum principal horizontal stress derived from this study is consistent with the results of GPS and geophysical studies of the northern Central Range (Hsu et al., 2009; Huang et al., 2012; Yeh et al., 2013). Since the strikes of the natural open fractures and the maximum principal horizontal stress are similar, the present-day regional tectonic stress field may at least partially control the developments and directions of natural open fractures which also have been observed in other tight reservoirs (Hennings et al., 2012; Jolie et al., 2014).

5.2.5. The foundation of the development of promising geothermal conduits

Based on the relations among lithology, fault displacement, fault activity, the direction of principal stress and the development of fractured structures, this study suggests that early-stage faulting penetrating thick brittle rocks, such as metasandstones or sandy slate, would be easier to develop promising geothermal fluid conduits in the slate belt. Thick formations with no faults, mature faults filled with fault gouges, healed faults, or faults pass through pure slate formations might not be effective fluid conduits for geothermal development.

5.3. The orientation and thickness of the fault system

As discussed in Subsection 5.1, Fault Zones 1–3 (800–1325 m MD) may represent a large-scale (major) fault system. For the sake of future geothermal exploration, this study used the orientations of both the deformed formations and open fractures to predict the lateral extension of the fault system beyond the borehole.

Due to fault dragging, orientations of formations along faults are often parallel or sub-parallel to the faults (Bengtson, 1981; Hesthammer and Fossen, 1998). The formation rotation in 1000–1350 m MD may be caused by the drags of faulting (Fig. 11). Therefore, the orientation of rotated formations, around N60–70 °E/70–90 °NW, should be parallel to the fault system. Second, the orientations of the permeable faults within the fault system, which are around N60–70 °E/70–90 °NW, could also be an indicator of the direction of faulting because of the orientation of the rotated formations and the permeable faults within the fault system are similar. The results of this study suggest that the orientation of the fault system is also N60–70 °E/70–90 °NW. The strike of the fault system is consistent with the "I" and "K" faults observed on the surface outcrops (Fig. 1).

The true width of the fault system could be calculated by the measured thickness of the fault system in the borehole, the orientation of the fault system, and the trajectory of wells by trigonometric conversions (Tearpock et al., 2003). By the calculation, this study found that
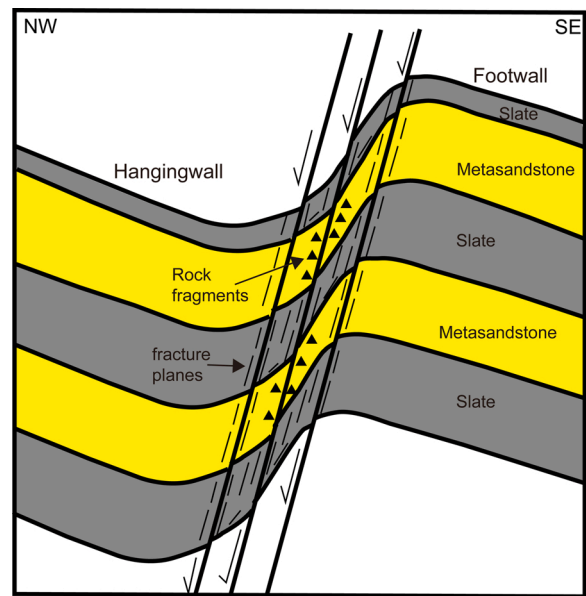

Fig. 11. The conceptual model of the fault system in this area. Because of the dragging along with the fault system, the orientations of beds have changed to be parallel or sub-parallel to the fault system. In the center of the fault system, the metasandstone tends to break into rock fragments, and fracture planes tend to develop in slate.

although the measured thickness of the major fault system in the JT-3 well was up to 485 m, the calculated true width of the fault system is only approximately 116 m because the well trajectory is sub-parallel to the fault system.

5.4. Petrophysical responses to the fracture developments

This study confirmed that open-hole logs respond to both the rock fracturing and lithological variations simultaneously. To observe how open-hole logs responding to the fractured structures independently, the lithological responses on logs are needed to be considered beforehand. This study used the GR (Vsh) log values as the indicator of lithology which was confirmed by the cutting data; then, we could observe how other open-hole logs responding to the fracturing in different lithology. It is important to know the fracturing tends to happen in low GR brittle rocks. The fracturing did not change the GR reading of the rocks.

First, this study divided the rocks into 1)metasandstone ($0 \leq \text{Vsh} \leq 0.3$), 2)sandy slate ($0.3 < \text{Vsh} \leq 0.7$), and 3)slate ($0.7 < \text{Vsh} \leq 1$) by Vsh for further comparisons. In the metasandstone and sandy slate categories, when the fracture intensities become higher (higher PHIE), the RT (in logarithmic scale) values would decrease in a linear trend (Fig. 12 (a) and (b)), and DT values would also increase (Fig. 13 (a) and (b)). However, in the slate category, because the fracture intensities are low (low PHIE log values), the RT and DT log values both only vary slightly and difficult to be separated from intact rocks (Fig. 12 (c) and Fig. 13 (c)). Besides, because of the low Vsh values in the fault cores with low RT, it indicates the fault cores are filled with low resistivity drilling mud, but not filled with low-resistivity radioactive clay-rich rock.

By the proposed procedures in this section and the demonstrations of Figs. 12 and 13, this study suggests the combinations of different open-hole logs could distinguish different intensities of fracturing in metasandstone and sandy-slate formations even if there are no FMI images of the boreholes. However, in high Vsh slate beds, the fracturing intensity may be low, and the open-hole responses to the fracturing would be hard to be identified.
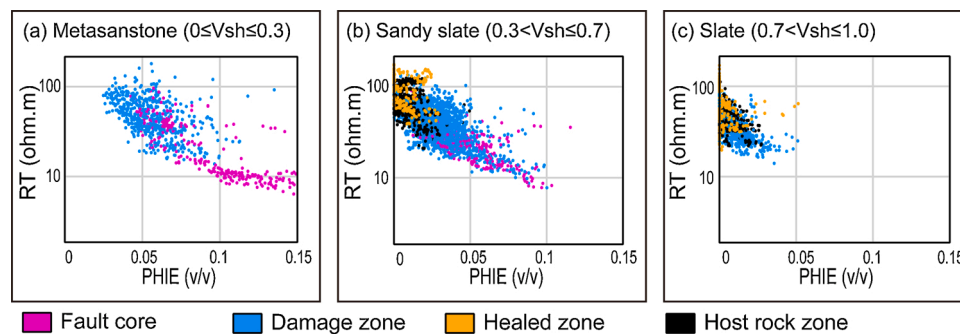
Fig. 12. The crossplot of PHIE and RT logs in different rock categories. The development of fault cores and damage zones made metasandstone (a) and sandy slate (b) to be more porous (lower RT and higher PHIE). However, the development of damage zones in slate did not make the RT and PHIE values change too much (c) because the fracture intensities are low in slate.
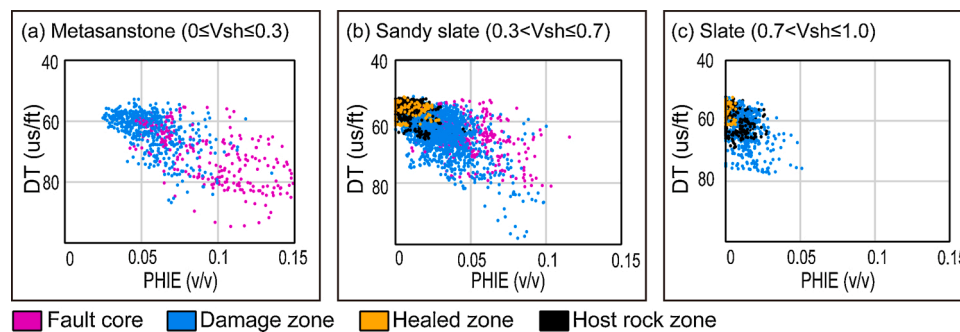

Fig. 13. The crossplot of PHIE and DT logs in different rock categories. The development of fault cores and damage zones made metasandstone (a) and sandy slate (b) to be more porous (high DT and higher PHIE). However, the development of damage zones in slate did not make the DT, and PHIE values change too much (c) because the fracture intensities are low in slate.

6. Conclusion

This study analyzed standard open-hole logs and FMI between 800–1475 m MD in well JT-3 to reveal the characteristics of fault-related fractures in the Jentse geothermal area in Northeastern Taiwan. The results showed that four fault zones pass through the studied interval.

Fault Zones 1–3 are permeable zones marked by porous brecciated fault cores and fault damage zones. Fault Zone 4 is a healed non-permeable fault zone marked by resistive fractures and resistive faults. The lithology by cuttings descriptions and the GR log both suggest the low resistivity and high neutron porosity of the fractured zones are caused by water-based drilling mud that infilled the fractures but not by precipitated clay minerals. The borehole temperature log also shows certain degrees of deflections in the intervals of the permeable zones that we interpreted by logs.

The results support the idea that the combination of Fault Zones 1–3 is a major permeable fault system in this geothermal area. The width of this major fault system is around 116 m, as inferred from the measured thickness in the borehole. By analyzing the orientations of beddings and fracture planes, it was determined that the fault system may strike N60–70 °N and dip 70–80 °N. The orientation is similar to the "I" or "K" faults at nearby surface outcrops. The inferred orientation of the fault system suggests the preferable extension areas for further geothermal explorations.

This study found that, within the fault system, the fracture characteristics between metasandstone and slate are different, both on open-hole and FMI logs. The metasandstone tended to be highly fractured and brecciated whereas the slate tended to form fracture planes or even remained intact. The fact that no thick fine-grained fault gouge layers have formed within the fault system suggests that the displacement of the fault system may be small. Based on the aforementioned observations, we believe that the development of geothermal fluid production

zones in this area may rely on the coexistence of faulting with small displacements and relatively brittle formations. However, if the faulting has stopped for a long period, these permeable fractures may have been gradually filled by cement and thus become non-permeable. We provide a distinct concept about how subsurface structures control geothermal conduits and can be applied in predicting possible geothermal prospects in fault-controlled geothermal areas.

Author statement

B.-C. Chen, T. Perdana, L.-W.K. wrote the paper; B.-C. Chen conceived the present idea; B.-C. Chen and T. Perdana analyzed the data; B.-C. Chen and T. Perdana contributed materials and analysis tools; all the authors part to the discussion. B.-C. Chen coordinated the study.

Declaration of Competing Interest

The authors report no declarations of interest.

Acknowledgments

References

Ameen, M.S., 2014. Fracture and in-situ stress patterns and impact on performance in the Khuff structural prospects, eastern offshore Saudi Arabia. Mar. Pet. Geol. 50, 166–184.

Barton, C.A., Zoback, M.D., 2002. Discrimination of natural fractures from drilling-induced wellbore failures in wellbore image data - implications for reservoir permeability. Spe Reserv. Eval. Eng. 5 (03), 249–254.

Bengtson, C.A., 1981. Statistical curvature analysis techniques for structural interpretation of dipmeter data. Am. Assoc. Pet. Geol. Bull. 65 (2), 312–332.

Bense, V.F., Gleeson, T., Loveless, S.E., Bour, O., Scibek, J., 2013. Fault zone hydrogeology. Earth-Sci. Rev. 127, 171–192.

Caine Jonathan, S., Evans James, P., Forster Craig, B., 1996. Fault zone architecture and permeability structure. Geology 24 (11), 1025–1028.

Chang, Y.K., Lee, H.S., Yang, J.H., Wu, G.H., Lee, J.Y., 1986. Geological Report of the Jentse and Tuchang Geothermal area, Ilan. CPC Corporation Taiwan, p. 24 in Chinese.

Chang, P.Y., Lo, W., Song, S.R., Ho, K.R., Wu, C.S., Chen, C.S., Lu, H.Y., 2014. Evaluating the Chingshui geothermal reservoir in northeast Taiwan with a 3D integrated geophysical visualization model. Geothermics 50, 91–100.

Chen, C.T., Chan, Y.C., Beyssac, O., Lu, C.Y., Chen, Y.G., Malavieille, J., et al., 2019. Thermal history of the northern taiwanese slate belt and implications for wedge growth during the neogene arc-continent collision. Tectonics 38 (9), 3335–3350.

Chiang, C.W., Hsu, H.L., Chen, C.C., 2015. An investigation of the 3D electrical resistivity structure in the Chingshui geothermal area, NE Taiwan. Terr. Atmos. Ocean. Sci. 26 (3), 269–281.

CPC, 1984. CPC-JT-2T Well Drilling Report. CPC Corporation Taiwan, p. 55. Chinese content.

Crain, P., 2013. Eng. Crain's Petrophysical Handbook [Internet].

Faulkner, D.R., Jackson, C.A.L., Lunn, R.J., Schlische, R.W., Shipton, Z.K., Wibberley, C.A.J., Withjack, M.O., 2010. A review of recent developments concerning the structure, mechanics and fluid flow properties of fault zones. J. Struct. Geol. 32 (11), 1557–1575.

Gray, M.B., Stamatakos, J.A., Ferrill, D.A., Evans, M.A., 2005. Fault-zone deformation in welded tuffs at Yucca Mountain, Nevada, USA. J. Struct. Geol. 27 (10), 1873–1891.

Hamahashi, M., Hamada, Y., Yamaguchi, A., Kimura, G., Fukuchi, R., Saito, S., Hashimoto, Y., 2015. Multiple damage zone structure of an exhumed seismogenic megasplay fault in a subduction zone - a study from the Nobeoka Thrust Drilling Project. Earth Planets Space 67 (1), 1–21.

Hennings, P., Allwardt, P., Paul, P., Zahm, C., Reid, R., Alley, H., Hough, E., 2012. Relationship between fractures, fault zones, stress, and reservoir productivity in the Suban gas field, Sumatra, Indonesia. AAPG Bull. 96 (4), 753–772.

Hesthammer, J., Fossen, H., 1998. The use of dipmeter data to constrain the structural geology of the Gullfaks Field, northern North Sea. Mar. Pet. Geol. 15 (6), 549–573.

Holland, M., Urai, J.L., van derZee, W., Stanjek, H., Konstanty, J., 2006. Fault gouge evolution in highly overconsolidated claystones. J. Struct. Geol. 28 (2), 323–332.

Houwers, M.E., Heijnen, L.J., Becker, A., Rijkers, R., 2015. a workflow for the estimation of fault zone permeability for geothermal production a General model applied on the roer Valley graben in the Netherlands. Proceedings World Geothermal Congress 2015 9 (April).

Hsiao, P.T., Chiang, S.C., 1979. Geology and geothermal system of the Chingshui-Tuchang geothermal area, Ilan, Taiwan. Pet. Geol. Taiwan 16, 205–213.

Hsu, Y.J., Yu, S.B., Simons, M., Kuo, L.C., Chen, H.Y., 2009. Interseismic crustal deformation in the Taiwan plate boundary zone revealed by GPS observations, seismicity, and earthquake focal mechanisms. Tectonophysics 479 (1–2), 4–18.

Huang, H.H., Shyu, J.B.H., Wu, Y.M., Chang, C.H., Chen, Y.G., 2012. Seismotectonics of northeastern Taiwan: kinematics of the transition from waning collision to subduction and postcollisional extension. J. Geophys. Res. Solid Earth 117 (1).

Jeppson, T.N., Bradbury, K.K., Evans, J.P., 2010. Geophysical properties within the San Andreas Fault Zone at the San Andreas Fault Observatory at depth and their relationships to rock properties and fault zone structure. J. Geophys. Res. Solid Earth 115 (12), 1–20.

Jolie, E., Moeck, I., Faulds, J.E., 2015. Quantitative structural-geological exploration of fault-controlled geothermal systems-A case study from the Basin-and-Range Province, Nevada (USA). Geothermics 54, 54–67.

Kuo, L.W., Song, S.R., Yeh, E.C., Chen, H.F., 2009. Clay mineral anomalies in the fault zone of the Chelungpu Fault, Taiwan, and their implication. Geophys. Res. Lett. 36, L18306.

Kuo, L.W., Song, S.R., Huang, L., Yeh, E.C., Chen, H.F., 2011. Temperature estimates of coseismic heating in clay-rich fault gouges, the Chelungpu fault zones, Taiwan. Tectonophysics 502, 315–327.

Kuo, L.W., Li, H., Smith, S., Di Toro, G., Suppe, J., Song, S.R., Nielsen, S., Sheu, H.S., Si, J., 2014. Gouge graphitization and dynamic fault weakening during the 2008 Mw 7.9 Wenchuan earthquake. Geology 42, 47–50. https://doi.org/10.1130/G34862.1.

Kuo, L.W., Di Felice, F., Spagnuolo, E., Di Toro, G., Song, S.-R., Aretusini, S., Li, H., Suppe, J., Si, J., Wen, C.-Y., 2017. Fault gouge graphitization as evidence of past seismic slip. Geology 45 (11), 979–982. https://doi.org/10.1130/G39295.1.

Lai, K.Y., Chen, Y.G., Wu, Y.M., Avouac, J.P., Kuo, Y.T., Wang, Y., Lin, K.C., 2009. The 2005 Ilan earthquake doublet and seismic crisis in northeastern Taiwan: evidence for dyke intrusion associated with on-land propagation of the Okinawa Trough. Geophys. J. Int. 179 (2), 678–686.

Lai, J., Wang, G., Wang, S., Cao, J., Li, M., Pang, X., et al., 2018. A review on the applications of image logs in structural analysis and sedimentary characterization. Mar. Pet. Geol. 95 (February), 139–166.

Lee, H.S., Lee, J.Y., 1983. Subsurface Geological Report of the CPC-JT-1T Geothermal Well in the Jentse Geothermal District I Lan. CPC Corporation Taiwan, p. 19. Chinese content.

Lin, C.H., 2000. Thermal modeling of continental subduction and exhumation constrained by heat flow and seismicity in Taiwan. Tectonophysics 324 (3), 189–201.

Lin, C.W., Lin, W.H., 1995. Explanatory Text of the Geologic Map of Taiwan Sanshin. Sheet 15. Cent. Geol. Surv. MOEA, Taiwan. Chinese content.

Liu, C.M., Song, S.R., Kuo, C.H., 2015. Silica geothermometry applications in the Taiwan orogenic belt. Terr. Atmos. Ocean. Sci. 26 (4), 387–396.

Lu, Y.C., Song, S.R., Wang, P.L., Wu, C.C., Mii, H.S., MacDonald, J., John, C.M., 2017. Magmatic-like fluid source of the Chingshui geothermal field, NE Taiwan evidenced by carbonate clumped-isotope paleothermometry. J. Asian Earth Sci. 149, 124–133.

Lu, Y.C., Song, S.R., Taguchi, S., Wang, P.L., Yeh, E.C., Lin, Y.J., John, C.M., 2018. Evolution of hot fluids in the Chingshui geothermal field inferred from crystal morphology and geochemical vein data. Geothermics 74 (June), 305–318.

Lu, Y.C., Song, S.R., Lin, P.H., Taguchi, S., Wang, C., Lai, Y.M., Lee, H.F., 2020. Thermal fluid changes after operating a geothermal system: a case study of the Chingshui Geothermal Field, Taiwan. Geothermics.

Luthi, S.M., Souhaite, P., 1990. Fracture apertures from electrical borehole scans. Geophysics.

Lyu, W., Zeng, L., Liao, Z., Ji, Y., Lyu, P., Dong, S., 2017. Fault damage zone characterization in tight-oil sandstones of the Upper Triassic Yanchang Formation in southwest Ordos Basin, China: integrating cores, image logs and conventional logs. Interpretation 5 (4).

Micarelli, L., Benedicto, A., Wibberley, C.A.J., 2006. Structural evolution and permeability of normal fault zones in highly porous carbonate rocks. J. Struct. Geol. 28 (7), 1214–1227.

Moeck, I.S., 2014. Catalog of geothermal play types based on geologic controls. Renew. Sustain. Energy Rev. 37, 867–882.

Peška, P., Zoback, M.D., 1995. Compressive and tensile failure of inclined wellbores and determination of in situ stress and rock strength. J. Geophys. Res. Solid Earth 100 (B7), 12791–12811.

Pöppelreiter, M., Crookbain, R.A., Sapru, A.K., Lawrence, M.J.F., 2010. Applications of dipmeter and borehole image data in static models. AAPG Memoir 92, 67–80.

Priest, S., 1993. Discontinuity Analysis for Rock Engineering. Springer, Netherlands.

Rawling, G.C., Goodwin, L.B., Wilson, J.L., 2001. Internal architecture, permeability structure, and hydrologic significance of contrasting fault-zone types. Geology 29 (1), 43–46.

Rowland, J.V., Sibson, R.H., 2004. Structural controls on hydrothermal flow in a segmented rift system, Taupo Volcanic Zone, New Zealand. Geofluids 4 (4), 259–283.

Schlumberger, 2015. Techlog Wellbore Imaging User Manual.

Shih, R.C., Wang, C.Y., Chen, W.S., Wang, Y.K., Kuo, H.Y., Yen, T.C., Chang, Y.F., 2018. Seismic reflection profiling of the first deep geothermal field in Taiwan. Geothermics 74, 255–272.

Shyu, J.B.H., Sieh, K., Chen, Y.G., Liu, C.S., 2005. Neotectonic architecture of Taiwan and its implications for future large earthquakes. J. Geophys. Res. Solid Earth 110 (8), 1–33.

Song, S.R., Lu, Y.C., 2019. Geothermal explorations on the slate formation of Taiwan. Renewable Geothermal Energy Explorations. IntechOpen.

Taguchi, S., Nakamura, M., 1991. Subsurface thermal structure of the Hatchobaru geothermal system, Japan, determined by fluid inclusion study. Geochem. J. 25 (4), 301–314.

Taillefer, A., Soliva, R., Guillou-Frottier, L., Goff, E.Le, Martin, G., Seranne, M., 2017. Fault-related controls on upward hydrothermal flow: an integrated geological study of the têt fault system, Eastern Pyrénées (France). Geofluids, 2017.

Tearpock, D.J., Bischke, R.E., Walker, L.G., 2003. Applied Subsurface Geological Mapping With Structural Methods. Prentice Hall PTR, Upper Saddle River, N.J.

Teng, L.S., 1996. Extensional collapse of the northern Taiwan mountain belt. Geology 24 (10), 949–952.

Terzaghi, R.D., 1965. Sources of error in joint surveys. Geotechnique 15 (3), 287–304.

Tong, L.T., Ouyang, S., Guo, T.R., Lee, C.R., Hu, K.H., Lee, C.L., Wang, C.J., 2008. Insight into the geothermal structure in Chingshui, Ilan, Taiwan. Terr. Atmos. Ocean. Sci. 19 (4), 413–424.

Tseng, C.S., 1978. Geology and geothermal occurrence of the Chingshui and Tuchang districts. Ilan. Pet. Geol. Taiwan 15, 11–23. Chinese content with English abstract.

Wallis, I.C., McNamara, D., Rowland, J.V., Massiot, C., 2012. The nature of fracture permeability in the basement greywacke at kawerau geothermal Field, New Zealand. In: Proceedings Thirty-Seventh Workshop on Geothermal Reservoir Engineering: Stanford University. Stanford, California p. SGP-TR-194.

Watkins, H., Healy, D., Bond, C.E., Butler, R.W.H., 2018. Implications of heterogeneous fracture distribution on reservoir quality; an analogue from the Torridon Group sandstone, Moine Thrust Belt, NW Scotland. J. Struct. Geol. 108, 180–197.

Wu, W.J., Kuo, L.W., Ku, C.S., Chiang, C.Y., Sheu, H.S., Aprilniadi, T.D., Dong, Jia-Jyun, 2020. Mixed-mode formation of amorphous materials in the creeping zone of the chihshang fault, Taiwan, and implications for deformation style. JGR Solid Earth. https://doi.org/10.1029/2020JB019862.

Yeh, E.C., Sun, T.H., Lin, S.T., Lee, W.C., Lin, W., Wu, Y.M., Wang, T.T., Song, S.R., Lin, W., 2013. Investigation of relationship between in-situ stress and fluid conduits from Chinshui geothermal area, NE Taiwan. AGU Fall Meeting H51D–1218.

Zoback, M.D., 2007. Reservoir Geomechanics. Reservoir Geomechanics. Cambridge University Press, Cambridge.